Journal of
Materials Chemistry A

Materials for energy and sustainability

Accepted Manuscript

This article can be cited before page numbers have been issued, to do this please use: S. Wang, Z. Li, F. Shen, Z. Ruan , Y. Huang, Y. Liu, Y. Liu, L. Chen, Y. Lan and Q. Zheng, *J. Mater. Chem. A*, 2023, DOI: 10.1039/D3TA01715J.

ROYAL SOCIETY OF CHEMISTRY

rsc.li/materials-a

DOI: 10.1039/D3TA01715J

MOF vertical array enables continuous ion transport pathways with high-throughput

Shuxian Wang,[a,1] Zhongliang Li,[a,1] Fangying Shen,[a,1] Zhiqin Ruan, Yutong Huang,[a] Yang Liu,[a] Yan Liu,[a] Luyi Chen,[a,*] Ya-Qian Lan,[a,*] and Qifeng Zheng[a,*]

[a] School of Chemistry, South China Normal University, 55 West Zhongsan Rd., Guangzhou 510006, Guangdong, China.
E-mail: chenluyi@m.scnu.edu.cn; yqlan@m.scnu.edu.cn; qifeng.zheng@m.scnu.edu.cn

[1] S. Wang, Z. Li, and F. Shen contributed equally to this work.

View Article Online
DOI: 10.1039/D3TA01715J

Abstract

Metal-organic frameworks (MOFs) have attracted a great deal of attention as ion conductive materials to design high-performance composite solid electrolytes (CSEs). However, sluggish Li^+ transport arising from the physical contact among MOF particles with numerous interfaces results in insufficient ionic conductivity and inhomogeneous Li deposition. Herein, a MOF array-based CSE is rationally proposed by embedding MOF vertical array with bilayer polymer electrolytes. The MOF vertical array offers not only continuous ion transport pathways with high-throughput and shortest transport distance, but also the open metal sites to anchor the anion and homogenize the Li^+ flux. Moreover, the bilayer polymer structure enhances the interfacial compatibility with Li-metal anode and high-voltage cathode simultaneously. Consequently, the resulting MOF array CSE endows the stable cycling of Li||Li symmetric cell for over 800 h and high-voltage Li||NCM cell at room temperature. Therefore, this work opens up new frontier in engineering CSE with MOF vertical array towards high-performance solid-state lithium batteries at room temperature.

View Article Online
DOI: 10.1039/D3TA01715J

1. Introduction

Lithium metal has been considered as the most promising anode for next-generation high-energy rechargeable lithium batteries due to its high theoretical specific capacity (3860 mAh g^{-1}) and the lowest electrochemical potential (−3.04 V *vs*. standard hydrogen electrode).[1-4] However, the conventional liquid organic electrolyte can spontaneously react with lithium metal anode,[5, 6] resulting in low Columbic efficiency (CE), high interfacial resistance, uneven Li^+ deposition, and uncontrollable growth of lithium dendrites, which can further cause short-circuit with serious safety issues.[7, 8] As a result, solid-state electrolytes (SSEs) have been gradually developed to address the aforementioned issues, owing to their desirable characteristics of being nonflammable and able to prevent the growth of lithium dendrites, as well as possessing a wide electrochemical voltage window.[9]

Up to now, various types of SSEs have been investigated, which can be classified as the following three categories, including inorganic solid electrolytes (ISEs), solid polymer electrolytes (SPEs), and composite solid electrolytes (CSEs).[10-14] ISEs, such as oxides (e.g., $Li_7La_3Zr_2O_{12}$, LLZO)[15] and sulfides (e.g., $Li_{10}GeP_2S_{12}$, LGPS[16]), possess the merits of high ionic conductivity at room temperature, good thermal stability and high Li^+ transference number,[17, 18] while their brittle nature leads to poor interfacial contact and poor processability.[19] While SPEs composed of polymeric matrixes (e.g., poly(vinylidene fluoride) (PVDF) or poly(ethylene oxide) (PEO)) with lithium salts, have been widely studied because of their high flexibility, excellent interface stability, and versatile processibility. However, SPEs suffer from poor mechanical strength and low ionic conductivity at room temperature, which hinders their practical applications.[20-22] Consequently, there is a growing interest in incorporating inorganic ionic conductors into the polymeric matrixes to formulate CSEs,

with the aim to combine the merits of ISEs and SPEs while overcoming their disadvantages.[23-25]

Recently, metal-organic frameworks (MOFs) have been served as a novel ionic conductor and shown great potential as fillers to manipulate ion transport in the CSEs.[26-28] Firstly, the high surface area of MOFs could improve interfacial contact with electrodes and electrolytes, endowing CSEs with low resistance. Secondly, the custom-made pores and the open metal sites (OMSs) from the functional framework of MOFs could capture the anions of lithium salts through the sieving effect and Lewis acid-base interaction, resulting in rapid Li^+ transport and high Li^+ transference number. Thirdly, the periodically ordered channels from MOFs could be helpful to achieve a homogeneous Li^+ flux and further regulate the homogenous deposition of Li.

However, as shown in Fig. 1a, by simply mixing MOF particles with SPEs, the MOF particles are isolated from each other that results in discontinuous Li^+ transport pathway, leading to inhomogeneous ion transport with insufficient ionic conductivity [29]. Recently, to overcome the issues of randomly distributed MOF particles in CSEs, many research efforts have been devoted to reduce the distance between discrete MOF particles with the aim to build a continuous ion transport pathway between MOFs[30-34] (Fig. 1b). For instance, by growing MOF (i.e., Zr-BPDC-2SO_3H) on bacterial cellulose nanofibers, a continuous ion transport network was built with the aid of propylene carbonate solvent (17.63 wt.%), which leads to a high ionic conductivity of 7.88×10^{-4} S cm^{-1} at 25 °C.[32] Later on, by in-situ growth of densely packed MOFs (i.e., ZIF-8) on polyacrylonitrile fibers and then encapsulating ionic liquid (IL) in the MOF pores, our group developed a MOF/IL-based CSE with a high ionic conductivity of 2.57×10^{-4} S cm^{-1} and a high Li^+ transference number of 0.59.[34] Howbeit, despite the successful construction of continuous Li^+ transport networks with significant reduced distance, the

View Article Online
DOI: 10.1039/D3TA01715J

point contact between different MOF particles would result in low throughput valve for Li^+ transport (Fig. 1b), leading to limited ionic conductivity improvement, unless the organic liquid is added (e.g., solvent or IL). Therefore, it is of great importance to build continuous ion transport pathways with high throughput and well-ordered structure to enable rapid Li^+ transport and homogeneous Li^+ flux (Fig. 1c).

Herein, a vertical aligned MOF array was rationally designed and embedded into the polymer electrolytes, which aims to afford continuous Li^+ transport pathway with high throughput. As illustrated in Fig. 2, the ingenious structure of MOF vertical array can regulate Li^+ transport along the shortest distance between the cathodes and anodes, promoting the fast transport of Li^+. Furthermore, the abundant OMSs from the framework of MOF array can capture the anions of lithium salts to offer homogeneous Li^+ flux, which increases the Li^+ transference number and thereby suppresses the growth of Li dendrites. After permeating the MOF vertical array with PVDF electrolyte and PEO electrolyte on both sides, the resultant MOF array CSE with bilayer polymer electrolytes demonstrates excellent interfacial compatibility towards both high-voltage cathode and Li-metal anode. Consequently, markedly improved cycling performance with high CE was realized for high-voltage Li||$LiNi_{1/3}Co_{1/3}Mn_{1/3}O_2$ (NCM) solid-state Li-metal battery at room temperature.

2. Experimental section

2.1. Synthesis of MOF vertical array

2.6 g of 2-methylimidazole and 1.17 g of $Co(NO_3)_2 \cdot 6H_2O$ were first dissolved in two 80 mL of deionized water, respectively. After stirring vigorously for 5 min, the above two solutions were mixed quickly. Then, the separator with a ceramic coating layer (MA-EN-SE-0D) was fixed on the beaker wall and further immersed in the mixed

View Article Online
DOI: 10.1039/D3TA01715J

solution for 5 h. After that, the separator with MOF (i.e., ZIF-67, $Co(mlm)_2$, mlm = 2-methylimidazole) array grown on the surface was taken out, washed with deionized water three times, and vacuum dried overnight. The mass loading of grown MOF array was measured to be about 1.26 mg cm^{-2}, which was calculated by measuring the weight of the separator before and after growing MOF array.

2.2. Fabrication of MOF array CSE

0.1 g of PVDF and 0.1 g of lithium bis(trifluoromethanesulphonyl)imide (LiTFSI) was first mixed in 2.0 ml of N-methylpyrrolidone (NMP) solvent, and then stirred for 6 hours at 50 °C to obtain a homogenous solution (denoted as PVDF/LiTFSI). The above PVDF/LiTFSI solution was coated on a clean and smooth glass plate using a 400 μm doctor blade. The separator with MOF array grown on top was then placed on the above PVDF/LiTFSI solution layer. A vacuum-assisted liquid filling method was employed to infiltrate the PVDF/LiTFSI into the MOF array, which was then vacuum dried at 80 °C for 24 h, and then the separator was peeled to afford the PVDF/MOF array. Thereafter, a mixed solution of PEO and LiTFSI (the molar ratio of [EO]: LiTFSI was 16:1) in acetonitrile with a concentration of 4.0 wt.% PEO was coated on the surface of PVDF/MOF array, and then subjected to vacuum dry at 80 °C for 24 h. The film was exfoliated from the glass substrate to yield a PVDF/MOF array/PEO CSE with bilayer polymer electrolytes on both sides (denoted as MOF array CSE). Finally, the film was cut into circular disc with a diameter of 19 mm and stored in a glove box prior to use.

2.3. Preparation of NCM cathode

The $LiNi_{1/3}Co_{1/3}Mn_{1/3}O_2$ (NCM) cathode was fabricated by mixing NCM powder with acetylene black and PVDF at a mass ratio of 80: 12: 8 using a Thinky mixer (AR-100).

View Article Online
DOI: 10.1039/D3TA01715J

The slurry was then coated on a clean and smooth aluminum foil with a 100 μm doctor blade and dried under vacuum at 100 °C for 24 h. The electrode was cut into 12 mm discs and further dried under vacuum at 60 °C for 24 h, and then placed in a glove box prior to use. The active mass loading of NCM cathode was controlled at 2-3 mg cm^{-2}.

2.4. Electrochemical measurements

All the cells, including stainless-steel (SS)||SS, Li||Li, Li||SS, and Li||NCM, were assembled in an Ar-filled glove box with a standard 2032-type coin cell configuration without any liquid electrolyte. Using a LAND CT2001A charge-discharge tester (Wuhan Jinnuo Electronic Co. Ltd.), the charge-discharge tests of the Li||Li symmetrical and Li||NCM cells were carried out at different current densities. The Li||NCM cells were tested with the cut-off voltage range of 2.8-4.3 V. The ionic conductivity of the CSE was measured by AC impedance spectrum with the CSE being placed between two stainless-steel (SS) blocking electrodes. The electrochemical impedance spectra were measured at the temperature range from 303 to 343 K with an amplitude of 10 mV within the frequency range of 10^6 to 0.1 Hz. The ion conductivity (σ) of CSE was calculated by the following equation:

$$\sigma = \frac{R}{L \times S} \quad (1)$$

where R is the bulk resistance, L is the thickness of CSE, and S is the area of CSE.

The oxidation stability of the CSE was measured via linear sweep voltammetry (LSV) at a sweep rate of 1.0 mV s^{-1} from open circuit voltage (OCV) to 6.0 V using SS as the working electrode and lithium metal as both reference and counter electrode. The Li^+ transference number (t_{Li^+}) were measured in a symmetric Li||Li cell according to the AC impedance and direct-current (DC) polarization (polarization voltage of 10 mV).

View Article Online
DOI: 10.1039/D3TA01715J

The t_{Li}^{+} was calculated from Bruce-Vincent-Evans equation:

$$t_{Li^+} = \frac{I_S \times (\Delta V - I_0 R_0)}{I_0 \times (\Delta V - I_S R_S)} \quad (2)$$

where I_0 and Is are the initial current and the steady state current, R_0 and Rs are charge-transfer resistance before and after polarization for 7200 s, and ΔV is the applied polarization voltage (ΔV = 10 mV). The ionic conductivity, LSV, and Li^+ transference number measurements were performed using a VMP3 potentiostat (Bio-Logic).

2.5. COMSOL simulation

The distribution of Li^+, $TFSI^-$, and electric potential through the CSEs was investigated based on Finite element method (FEM)[35] using COMSOL Multiphysics. Two physical models of electrostatic and transport of diluted species based on the partial differential equations were coupled to conduct FEM simulation. The CSEs were built into a two-dimensional plane model, where the upper and lower surfaces were contacted boundaries between the CSEs and Li metal electrodes. The migration of Li^+ and $TFSI^-$ were described by Nernst-Planck equation. The diffusion coefficients of Li^+ and $TFSI^-$ in MOF array CSE were 7.48×10^{-10} cm^2 S^{-1} and 6.12×10^{-10} cm^2 S^{-1}, respectively. For MOF particle CSE, the diffusion coefficients of Li^+ and $TFSI^-$ were 2.81×10^{-10} cm^2 S^{-1} and 9.40×10^{-10} cm^2 S^{-1}, respectively. Current density was set as 0.2 mA cm^{-2} and a temperature of 303 K was applied.

View Article Online
DOI: 10.1039/D3TA01715J

3. Results and discussion

3.1. Rational design and fabrication of MOF array CSE

Introducing crystalline MOFs as fillers into polymeric electrolytes has been regarded as a promising strategy to achieve high performance CSEs, in which the high specific surface areas of MOFs can facilitate contact with polymer to reduce the interfacial resistance, the OMSs of MOFs can anchor anions of Li salts to promote rapid Li^+ transport and high Li^+ transference, the periodically ordered channels of MOFs are favorable to generate homogeneous Li^+ flux to induce homogeneous Li^+ plating/stripping. However, due to the discrete MOF particles in polymeric matrix (Fig. 2a), Li^+ was primarily transported via MOF-to-polymer-to-MOF, which leads to high interfacial resistance and sluggish Li^+ transport.

As shown in Fig. 2b, aiming to build a continuous Li^+ transport pathway with the shortest transport distance between cathode and anode, a MOF vertical array-based CSE was rationally designed that is free of crossing junctions with low Li^+ migration barrier. The procedure to fabricate MOF array CSE with bilayer polymer electrolytes is schematically shown in Figure 3a. The separator with a ceramic coating layer serves as an excellent substrate for the growth of MOF (i.e., ZIF-67) vertical array. The top view scanning electron microscopy (SEM) image demonstrates that the MOF array with typical vertical aligned morphology was uniformly grown on the separator (Fig. 3b), and the thickness of MOF array was about 17 μm according to the cross-sectional SEM image (Fig. 3c), which is expected to offer continuous and rapid ion transport pathways. The X-ray diffraction (XRD) pattern of MOF array/separator well matches with the pristine separator and pure MOF particle (i.e., ZIF-67, Fig. S1), which is also consistent with earlier work in literature.[36, 37] In addition, the corresponding elemental mapping images in Fig. S2-S3 displays homogeneous elemental distribution of Co, C,

View Article Online
DOI: 10.1039/D3TA01715J

and N. These results demonstrate the successful construction of ZIF-67 vertical array on the separator substrate.

The MOF array/separator is then infiltrated with PVDF by doctor-blading PVDF/LiTFSI solution on a piece of glass plate and then placing the MOF/separator on the solution film with the MOF array side facing the solution. With the assistance of vacuum, the voids among MOF array were permeated through with PVDF/LiTFSI. To improve the interfacial compatibility of CSE with Li-metal anode, an additional PEO electrolyte layer is then casted on the PVDF/MOF array. The MOF array CSE with a hierarchical structure is finally obtained with a 15 μm thick PVDF layer and a 5.0 μm thick PEO layer permeating the MOF array (Fig. 3d), where the MOF array is expected to provide continuous and shortest Li^+ transport pathways, the high-voltage tolerance PVDF layer can be well compatible with high-voltage cathode, and the PEO layer is expected to be well compatible with Li-metal anode. For comparison, the MOF particles randomly distributed CSE (denoted as MOF particle CSE) with similar bilayer polymer electrolytes was also prepared (Fig. S4). The mass loading of MOF in both MOF array CSE and MOF particle CSE was controlled at ~1.25 mg cm^{-2}. From the SEM images in Fig. S5, although there are some protrusions on the surface resulting from the vertical growth of MOF array, the MOF array CSE was thoroughly infiltrated with PVDF/LiTFSI and PEO/LiTFSI. Furthermore, since rigorous drying protocol was applied during the fabrication, we assume that both MOF array CSE and MOF particle CSE do not contain any liquid, which was verified by the negligible weight loss before 225 °C during the thermogravimetric analysis (TGA) test (Fig. S6).

3.2. Physicochemical properties of MOF array CSE

The ionic conductivity is the primarily parameter to evaluate the properties of CSEs

View Article Online
DOI: 10.1039/D3TA01715J

for their practical application in solid-state Li-metal batteries, which was calculated from the AC impedance spectra. As shown in the Fig. S7, the ionic conductivity of the MOF array CSE without any liquid electrolyte was up to 1.12×10^{-4} S cm^{-1} at 30 °C, which is one order of magnitude higher than that of MOF particle CSE (5.92×10^{-5} S cm^{-1}), indicating that the structure of MOF vertical array with continuous and shortest ion transport pathways can evidently promote the Li^+ transport. Furthermore, the activation energies (E_a) of CSEs can be obtained from the Arrhenius equation. As shown in Fig. 3e, the E_a of MOF array CSE was calculated to be 0.23 eV, which is lower than that of MOF particle CSE (0.32 eV), indicating that a lower Li^+ migration energy barrier was realized in MOF array CSE. The high ionic conductivity and low energy barrier for Li^+ migration in MOF array CSE can be ascribed to the continuous ion transport pathways and shortest transport distance offered by MOF array structure (Fig. 2b), favoring their application at room temperature. While the poor interfacial contact through physical mixing MOF particles with polymer electrolytes CSE results in discontinuous ion transport pathway and hinders Li^+ migration, leading to low ionic conductivity and high migration barrier (Fig. 2a).

According to the space-charge model demonstrated by Chazalviel,[38, 39] in which lithium dendrites would grow when the Li^+ concentration on the surface of the electrode falls to zero at a high current density. The initial time of lithium dendrite growth is called Sand's time (τ), which empirically relies on the electron and Li^+ transference number (t_{Li}^+). A higher t_{Li}^+ would generate a higher limiting current that postpones the Sand's time, inhibiting the growth of lithium dendrites. Thus, as shown in Fig. 3f and S8, the t_{Li}^+ was evaluated by the AC impedance and direct-current (DC) polarization. The t_{Li}^+ of the MOF array CSE was calculated to be 0.55, which is much higher than that of the MOF particle CSE (0.23). This was attributed to the continuous ion transport

View Article Online
DOI: 10.1039/D3TA01715J

pathways with high throughput and shortest transport distance processed by MOF array that promotes the rapid transport of Li^+, in addition to the abundant open metal sites and sieving effect offered by MOF that can effectively restrict the $TFSI^-$ anion.

Furthermore, the electrochemical stability window of CSEs at room temperature was crucial for their application in high-voltage lithium batteries, which was measured by the linear sweep voltammetry (LSV). As shown in Fig. 3g, MOF array CSE shows a high oxidation potential of 4.53 V, which is much higher than that of the MOF particle CSE (4.19 V) defined at 0.001 mA cm^{-2}. The superior oxidation stability of the MOF array CSE was attributed to the continuous ion transport pathway with high throughout and shortest transport distance offered by MOF array, enabling the majority of charges to transport along the continuous MOF pathways while minimizing the charge transport across the polymer matrixes.

3.3. Homogeneous Li deposition

The Li||Li symmetric cells using various CSEs were configured and tested to evaluate the long-term electrochemical stability and polarization during the Li plating/stripping process. As shown in Fig. 4a, after three activation cycles at the current density of 0.1 mA cm^{-2} with each plating/stripping procedure of 1 h, the Li||Li symmetric cell using MOF particle CSE experiences apparent short circuit after about 400 h at a current density of 0.2 mA cm^{-2} for 0.2 mAh cm^{-2} due to the overgrowth of lithium dendrites, while the cycling life was extended to over 800 h with a small and steady polarization voltage of 72 mV for that of using MOF array CSE. This result suggests that MOF array CSE with continuous and high throughput Li^+ transport pathway could markedly regulate the homogeneous Li^+ deposition, which was confirmed by the flat and smooth surface of lithium metal anode without obvious lithium dendrite after 100 hours from

View Article Online
DOI: 10.1039/D3TA01715J

SEM image in Fig. 4c. Whereas the lithium metal anode cycled using MOF particle CSE displays a rough surface with bushy lithium dendrite, as shown in the SEM image in Fig. 4b. Moreover, compared with the significantly increased interfacial impedance in the symmetric Li||Li cell using MOF particle CSE during cycling (Fig. 4d), the interfacial impedance of the cell coupling with MOF array CSE exhibits negligible increase during cycling (Fig. 4e), indicating its excellent interfacial stability. Furthermore, the Li||Li symmetric cells using MOF array CSE can also support the stable cycling at high current densities (Fig. S9), i.e., more than 450 h at 0.3 mA cm^{-2} with a capacity of 0.3 mAh cm^{-2} and more than 300 h at 0.5 mA cm^{-2} with a capacity of 0.5 mAh cm^{-2}, respectively.

These results demonstrate that constructing continuous and high throughput Li^+ transport pathway based on MOF array with a high aspect ratio is favorable for realizing dendrite-free Li plating/stripping, attributing to the following reasons as schematically summarized in Fig. 4f: 1) due to the high aspect ratio of MOF array, Li^+ could transport rapidly along the long-range and periodical order channels; 2) MOF array as the homogeneous filler possesses ion transport pathway with high throughput and shortest distance give rise to homogeneous Li^+ flux, thereby regulating homogeneous Li^+ deposition; 3) the microporous structure and abundant OMSs within MOF could restrict the $TFSI^-$ anion to increase Li^+ transference number, therefore suppressing the growth of lithium dendrites and resulting in a dendrite-free Li plating/stripping.

To further illuminate the ion transport trajectory in MOF array CSE, the distribution of Li^+, $TFSI^-$, and electric field in the Li||Li symmetric cell were simulated by COMSOL Multiphysics. As shown in Fig. 5a and 5b, both Li^+ and $TFSI^-$ show small concentration gradients during the process of Li^+ plating in MOF array CSE, indicating homogeneous Li^+ flux, which was primarily ascribed to its high t_{Li^+} as well as

continuous and rapid Li^+ transport pathway. Because of the uniform distribution of Li^+ and $TFSI^-$, a small potential field is also observed for MOF array CSE (Fig. 5c), enabling uniform and dendrite-free Li deposition. In contrast, the MOF particle CSE shows large concentration gradients for Li^+ and $TFSI^-$ as well as large potential field (Figs. 5d-f), which results in uneven Li^+ deposition and rapid growth of lithium dendrites.

3.4. Stable operation of high voltage Li||NCM cell

The superiority of MOF array CSE with continuous ion transport pathways and a hierarchical structure is eventually subjected to test of high-voltage Li||NCM cells at 30 °C with a cutoff voltage of 2.8-4.3 V. As shown in Fig. 6a, the Li||NCM cell using MOF array CSE delivers excellent rate capability, where the discharge capacities were 154, 146, 128, and 105 mAh g^{-1} at 0.1, 0.2, 0.5, and 1 C, respectively. When the current density came back to 0.2 C, the discharge capacity recovers to 148 mAh g^{-1}, indicating its excellent rate capability at room temperature, which could be attributed to its high ionic conductivity and high t_{Li^+} as well as very thin nature of the CSE (~20 μm). In sharp contrast, the Li||NCM cell using MOF particle CSE shows lower discharge capacities at various current densities. Furthermore, the Li||NCM cell using MOF array CSE also shows lower over-potentials (e.g., 416 mV at 1 C) than that of using MOF particle CSE (560 mV at 1 C) in charge-discharge curves (Figs. 6b and S10).

The long-term cycling performance of the Li||NCM cells were also tested. As shown in Fig. 6c, the Li||NCM cell using MOF array CSE displays a stable cycling performance with an initial discharge capacity of 137 mAh g^{-1} and a capacity retention of 75% after 300 cycles, outperforming most of reported high-voltage cells (i.e., >4.0 V) using MOFs/polymer based CSEs without any liquid (Table S1). While the Li||NCM

View Article Online
DOI: 10.1039/D3TA01715J

cell using MOF particle CSE can only survive for 160 cycles, which may be ascribed to its poor oxidative stability. Furthermore, the surface morphology of cycled lithium metal anode after 100 cycles was also investigated and shown in Fig 6c. The cycled lithium metal anode using MOF array CSE exhibits smooth and dendrite-free morphology, while that using MOF particle CSE displays massive porous and mossy-like morphology, indicating that the growth of the lithium dendrite has been effectively prevented by the deliberate construction of MOF array with continuous and rapid Li^+ transport pathways, high Li^+ transference number, and homogeneous Li^+ flux.

Moreover, compared with that of using MOF particle CSE in Fig. 6d, the Li||NCM cell using MOF array CSE exhibits no obvious change in the voltage polarization during cycling (Figure 6e), suggesting its excellent interfacial compatibility towards both cathode and anode, which was further evidenced by the electrochemical impedance measurement (Fig. S11). In contrast to the cell using MOF particle CSE, whose interfacial resistance drastically increased after 10 cycles, the cell using MOF array CSE displays impressively steady interfacial resistance even after 300 cycles. Additionally, the Li||NCM cell using MOF array CSE also demonstrates stable cycling at high current density of 0.5 C at 60 °C, while the cell using MOF particle CSE exhibits rapid capacity decay (Fig. S12).

4. Conclusions

In summary, a MOF array CSE was delicately designed by embedding vertical MOF array with bilayer polymer electrolytes to overcome the longstanding challenges of large Li^+ migration barrier, inhomogeneous Li deposition, and high-voltage incompatibility. The MOF vertical array cannot only offer continuous ion transport pathway with high-throughput, but also minimize the Li^+ transport distance between

View Article Online
DOI: 10.1039/D3TA01715J

cathode and anode. Furthermore, the utilization of MOF array with open metal sites and periodical ordered channel can restrict anion transport to achieve homogeneous Li^+ flux with high Li^+ transference number (0.55). Moreover, the unique bilayer structure is demonstrated to stabilize both Li-metal anode and high-voltage cathode. Benefiting from the above merits, the resulting MOF array CSE endows the stable cycling of Li||Li symmetric cell for over 800 h and high-voltage Li||NCM cell at room temperature. This work highlights the great prospect for constructing MOF array with continuous ion transport pathways and shortest transport distance in CSEs, which opens up a new avenue for the development of high-performance solid-state batteries.

View Article Online
DOI: 10.1039/D3TA01715J

Conflicts of interest

There are no conflicts to declare.

Acknowledgements

This work was supported by the National Natural Science Foundation of China (Nos. 22005108, 22208118), Natural Science Foundation of Guangdong Province (Nos. 2021A1515110655, 2022B1515020005), Department of Science and Technology of Guangdong Province (Nos. 2021A0505030063, 2020B0101030005).

View Article Online
DOI: 10.1039/D3TA01715J

References

1. D. T. Boyle, X. Kong, A. Pei, P. E. Rudnicki and Y. Cui, *ACS Energy Lett.*, 2020, **5**, 701-709.
2. X. B. Cheng, R. Zhang, C. Z. Zhao and Q. Zhang, *Chem. Rev.*, 2017, **117**, 10403-10473.
3. S. Jin, Y. Ye, Y. Niu, Y. Xu, H. Jin, J. Wang, Z. Sun, A. Cao, X. Wu and Y. Luo, *J. Am. Chem. Soc.*, 2020, **142**, 8818-8826.
4. X. R. Chen, B. C. Zhao, C. Yan and Q. Zhang, *Adv. Mater.*, 2021, **33**, 2004128.
5. J. F. Ding, R. Xu, X. X. Ma, Y. Xiao, Y. X. Yao, C. Yan and J. Q. Huang, *Angew. Chem. Int. Ed.*, **61**, e202115602.
6. B. Liu, J. G. Zhang and W. Xu, *Joule*, 2018, **2**, 833-845.
7. K. Amine, R. Kanno and Y. Tzeng, *MRS Bulletin*, 2014, **39**, 395-401.
8. X. Wu, J. L. Wang, D. Fei, X. L. Chen, E. Nasybulin, Y. H. Zhang and J. G. Zhang, *Energy Environ. Sci.*, 2014, **7**, 513-537.
9. R. Chen, Q. Li, X. Yu, L. Chen and H. Li, *Chem. Rev.*, 2020, **120**, 6820–6877.
10. J. C. Bachman, S. Muy, A. Grimaud, H. H. Chang and Y. Shao-Horn, *Chem. Rev.*, 2015, **116**, 140-162.
11. J. Wan, J. Xie, D. G. Mackanic, W. Burke and Y. Cui, *Mater. Today Nano*, 2018, **4**, 1-16.
12. S. X. Xia, X. S. Wu, Z. C. Zhang, Y. Cui and W. Liu, *Chem*, 2019, **5**, 753–785.
13. Y. Zheng, Y. Z. Yao, J. H. Ou, M. Li and Z. W. Chen, *Chem. Soc. Rev.*, 2020, **49**, 8790–8839.
14. D. Zhou, D. Shanmukaraj, A. Tkacheva, M. Armand and G. Wang, *Chem*, 2019, **5**, 2326–2352.
15. X. Zhan, S. Lai, M. P. Gobet, S. G. Greenbaum and M. Shirpour, *Phys. Chem. Chem. Phys.*, 2018, **20**, 1447-1459.
16. Y. Sun, K. Suzuki, K. Hara, S. Hori, T. A. Yano, M. Hara, M. Hirayama and R. Kanno, *J. Power Sources*, 2016, **324**, 798-803.
17. J. R. Xu, L. L. Liu, N. Yao, F. Wu and L. Q. Chen, *Mater. Today Nano*, 2019, **8**,

View Article Online
DOI: 10.1039/D3TA01715J

100048.

18. D. Zhou, M. Y. Zhang, F. Sun, T. Arlt and M. Winter, *Nano Energy*, 2020, **77**, 105196.
19. S. S. Chi, Y. Liu, N. Zhao, X. Guo, C. W. Nan and L. Z. Fan, *Energy Storage Mater.*, 2019, **17**, 309-316.
20. O. Borodin and G. D. Smith, *Macromolecules*, 2006, **39**, 1620-1629.
21. S. H. Cheng, K. He, Y. Liu, J. W. Zha, M. Kamruzzaman, L. W. Ma, Z. Dang and C. Y. Chung, *Electrochim. Acta*, 2017, **253**, 430-438.
22. M. Nishiura, M. Kono, N. Namegaya and Y. Matsuda, *Electrochem. Solid-State Lett.*, 1998, **1**, 246-248.
23. X. Han, Y. Gong, K. K. Fu, X. He, G. T. Hitz, J. Dai, A. Pearse, B. Liu, H. Wang, G. Rubloff, Y. Mo, V. Thangadurai, E. D. Wachsman and L. Hu, *Nat. mater.*, 2017, **16**, 572-579.
24. J. Liang, J. Luo, Q. Sun, X. Yang and X. Sun, *Energy Storage Mater.*, 2019, **21**, 308-334.
25. Q. Zhou, J. Ma, S. Dong, X. Li and G. Cui, *Adv. Mater.*, 2019, **31**, 1902029.
26. S. Bai, Y. Sun, J. Yi, Y. He, Y. Qiao and H. Zhou, *Joule*, 2018, **2**, 2117-2132.
27. W. Xu, X. Pei, C. S. Diercks, H. Lyu and O. M. Yaghi, *J. Am. Chem. Soc.*, 2019, **141**, 17522–17526.
28. R. Zhao, Y. Wu, Z. Liang, L. Gao, W. Xia, Y. Zhao and R. Zou, *Energy Environ. Sci.*, 2020, **13**, 2386-2403.
29. L. Chen, K. Ding, K. Li, Z. Li, X. Zhang, Q. Zheng, Y.-P. Cai and Y.-Q. Lan, *EnergyChem*, 2022, **4**, 100073.
30. L. Du, B. Zhang, W. Deng, Y. Cheng, L. Xu and L. Mai, *Adv. Energy Mater.*, 2022, **12**, 2200501.
31. Z. Li, S. Wang, J. Shi, Y. Liu, S. Zheng, H. Zou, Y. Chen, W. Kuang, K. Ding, L. Chen, Y.-q. Lan, Y.-p. Cai and Q. Zheng, *Energy Stor. Mater.*, 2022, **47**, 262-270.
32. Q. Zeng, J. Wang, X. Li, Y. Ouyang, W. He, D. Li, S. Guo, Y. Xiao, H. Deng, W. Gong, Q. Zhang and S. Huang, *ACS Energy Lett.*, 2021, **6**, 2434-2441.
33. Q. Zhang, B. Liu, J. Wang, Q. Li, D. Li, S. Guo, Y. Xiao, Q. Zeng, W. He, M.

View Article Online
DOI: 10.1039/D3TA01715J

Zheng, Y. Ma and S. Huang, *ACS Energy Lett.*, 2020, **5**, 2919-2926.

34. X.-L. Zhang, F.-Y. Shen, X. Long, S. Zheng, Z. Ruan, Y.-P. Cai, X.-J. Hong and Q. Zheng, *Energy Stor. Mater.*, 2022, **52**, 201-209.
35. J. Newman, K. E. Thomas, H. Hafezi and D. R. Wheeler, *J. Power Sources*, 2003, **119**, 838-843.
36. G. Fang, J. Zhou, C. Liang, A. Pan, C. Zhang, Y. Tang, X. Tan, J. Liu and S. Liang, *Nano Energy*, 2016, **26**, 57-65.
37. C. Guan, W. Zhao, Y. Hu, Z. Lai, X. Li, S. Sun, H. Zhang, A. K. Cheetham and J. Wang, *Nanoscale Horiz.*, 2017, **2**, 99-105.
38. J. N. Chazalviel, *Phys. Rev. A*, 1991, **42**, 7355-7367.
39. X. Zhang, A. Wang, X. Liu and J. Luo, *Acc. Chem. Res.*, 2019, **52**, 3223-3232.
40. M. Yao, T. Yu, Q. Ruan, Q. Chen, H. Zhang and S. Zhang, *ACS Appl. Mater. Interfaces*, 2021, **13**, 47163–47173.
41. Z. Li, S. Wang, J. Shi, Y. Liu, S. Zheng, H. Zou, Y. Chen, W. Kuang, K. Ding, L. Chen, Y. Lan, Y. Cai and Q. Zheng, *Energy Stor. Mater.*, 2022, **47**, 262-270.

View Article Online
DOI: 10.1039/D3TA01715J

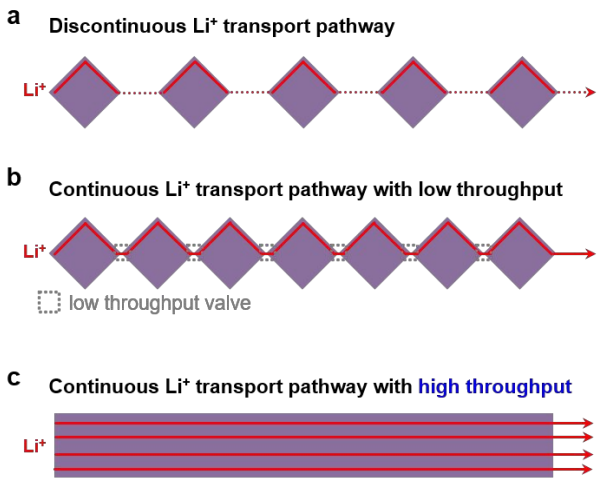

Fig. 1. The comparison of possible Li^+ transport pathways in various MOF-based CSEs. Schematic illustration of Li^+ transport pathways in CSEs with (a) randomly distributed MOF particles, (b) closely packed MOF particle-based chains reported recently, and (c) aligned MOF arrays proposed in this study. Compared with randomly distributed MOF particles, closely packed MOF chains offer a more continuous Li^+ transport pathway, but suffer from low throughput. While the proposed MOF arrays are free of crossing junctions with high throughput, thus enabling rapid Li^+ transport.

View Article Online
DOI: 10.1039/D3TA01715J

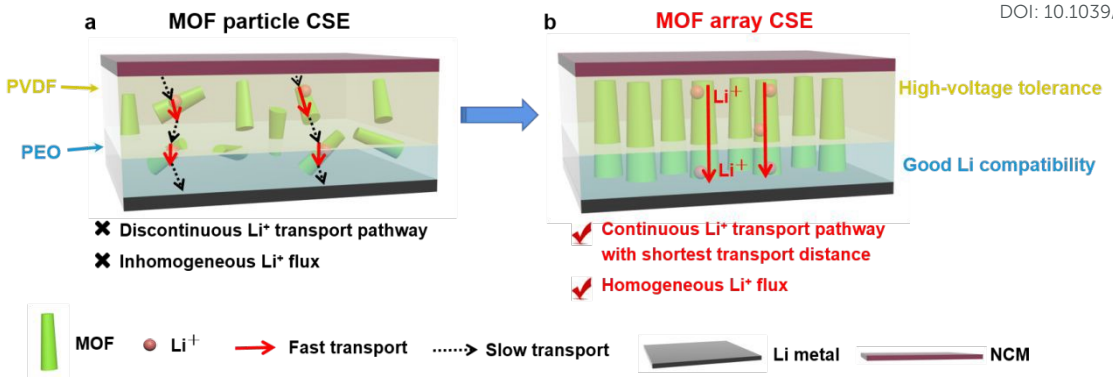

Fig. 2. Schematic illustrations of the Li^+ transport behaviors in (a) MOF particle CSE and (b) MOF array CSE. The discrete MOF particles in MOF particle CSE result in discontinuous Li^+ transport pathway with inhomogeneous Li^+ flux. While the MOF array CSE not only offers continuous Li^+ transport pathway with shortest transport distance between cathode and anode, but also contributes to homogeneous Li^+ flux.

View Article Online
DOI: 10.1039/D3TA01715J

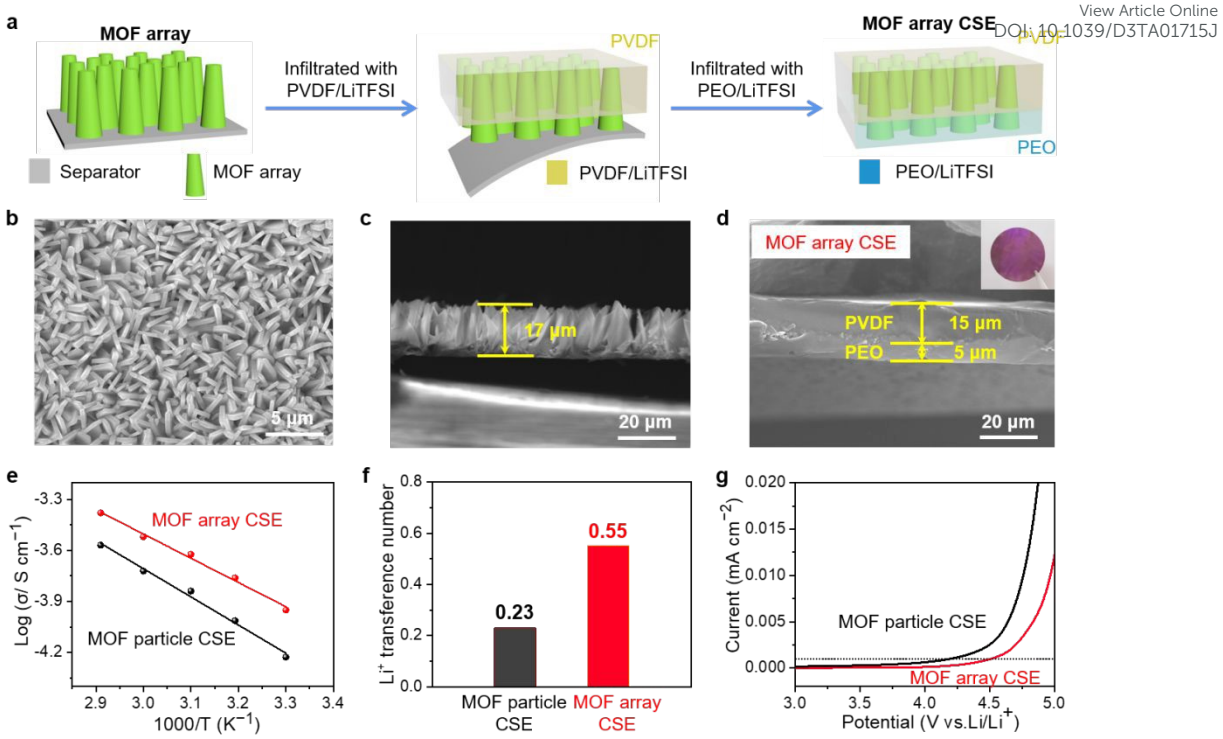

Fig. 3. Preparation and characterizations of the CSEs. (a) Schematic procedure to fabricate the MOF array CSE. (b) Top view and (c) cross-sectional view of SEM images of MOF array grown on the separator. (d) Cross-sectional view of MOF array CSE with bilayer polymer electrolytes. (e) Temperature-dependent ionic conductivities, (f) Li^+ transference numbers, and (g) oxidative stabilities of the MOF particle CSE and MOF array CSE.

View Article Online
DOI: 10.1039/D3TA01715J

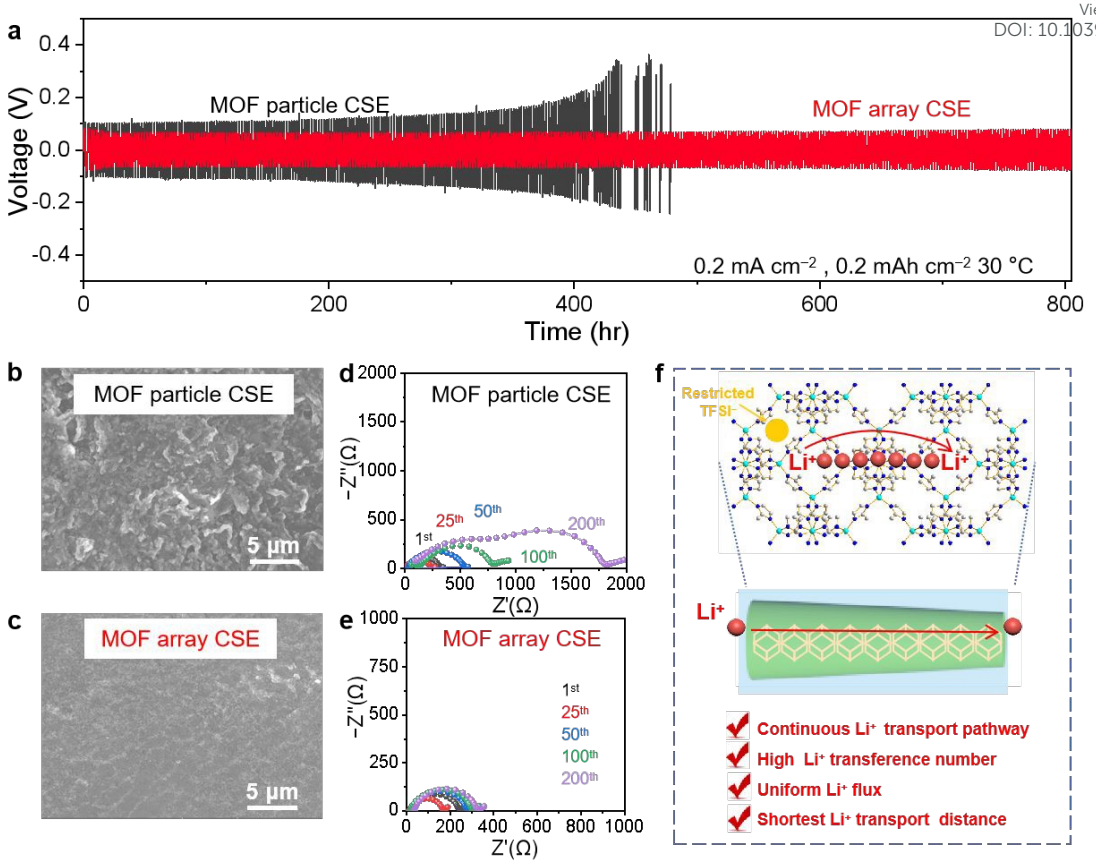

Fig. 4. Li plating/stripping stability. (a) Long-term cycling stability of symmetric Li||Li cells at a current density of 0.2 mA cm^{-2} for 0.2 mAh cm^{-2} at 30 °C. SEM images of Li-metal recovered from symmetric Li||Li cells using (b) MOF particle CSE and (c) MOF array CSE after 200 cycles. Electrochemical impedance spectra of symmetric Li||Li cells using (d) MOF particle CSE and (e) MOF array CSE after different cycles at 30 ℃. (f) Schematic illustration of ion transport behavior with a MOF array CSE, where the MOF array offers a continuous and rapid ion transport pathway with shortest distance, leading to homogeneous Li^+ flux and high Li^+ transference number.

View Article Online
DOI: 10.1039/D3TA01715J

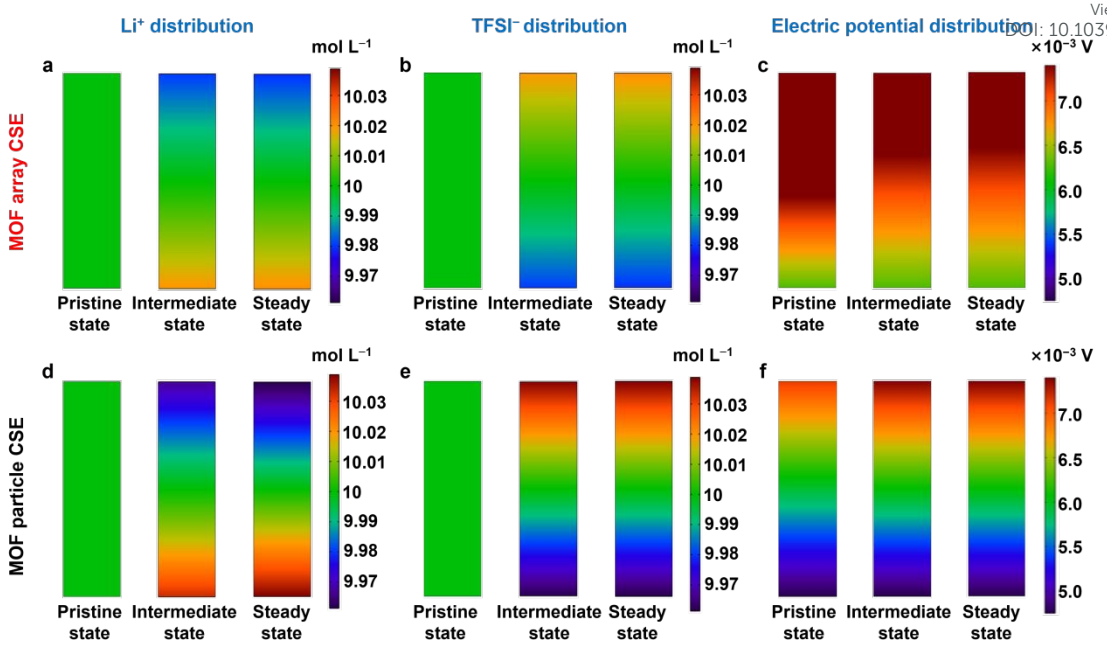

Fig. 5. COMSOL simulation results. The Li^+, $TFSI^-$, and electric potential distribution in (a-c) MOF array CSE and (d-f) MOF particle CSE at pristine, intermediate, and steady states during Li^+ deposition at a current density of 0.2 mA cm^{-2}.

View Article Online
DOI: 10.1039/D3TA01715J

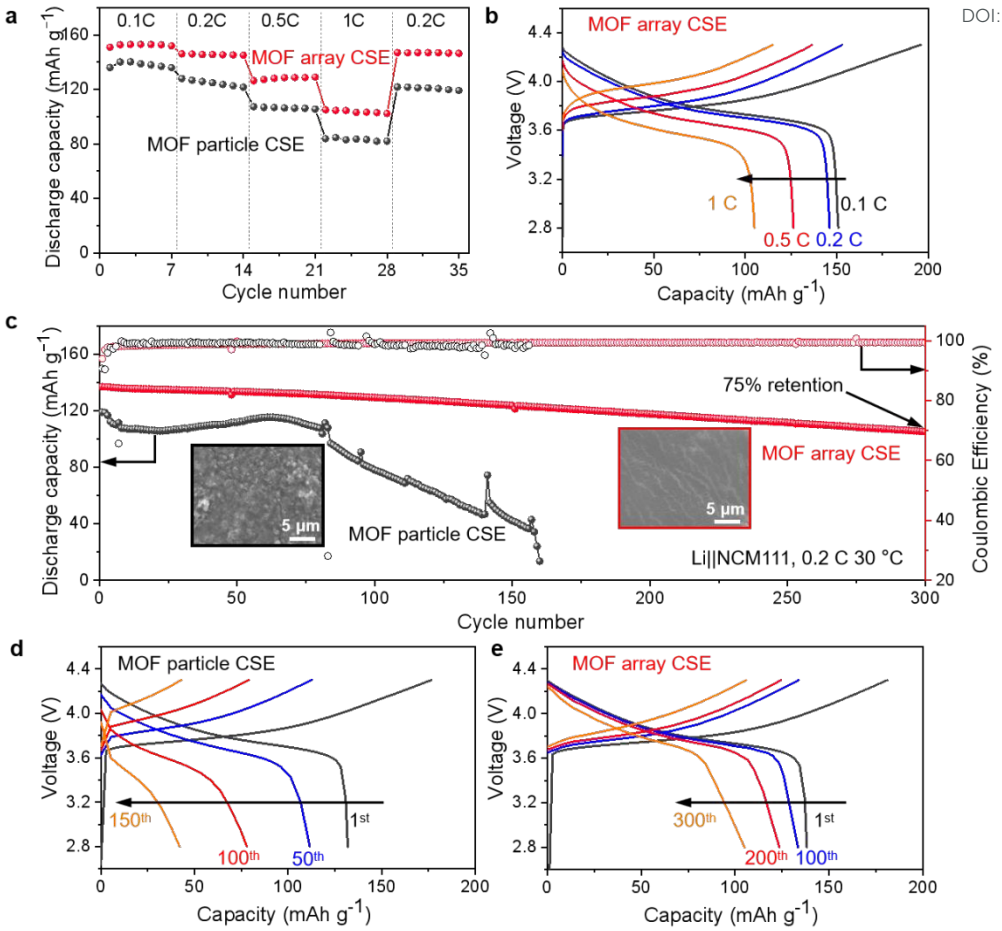

Fig. 6. Electrochemical performance of the Li||NCM cells at 30 °C. (a) Rate performance of Li||NCM cells using MOF particle and MOF array CSEs. (b) Selected charge-discharge curves of Li||NCM cell using MOF array CSE at different current densities. (c) Cycling performance and (d, e) selected charge-discharge curves of Li||NCM cells using MOF particle and MOF array CSEs with a cut-off voltage of 2.8-4.3 V at 0.2 C.